Merging Parametric Active Contours Within Homogeneous Image Regions for MRI-Based Lung Segmentation

Nilanjan Ray, *Student Member, IEEE*, Scott T. Acton*, Talissa Altes, Eduard E. de Lange, and James R. Brookeman

***Abstract*—Inhaled hyperpolarized helium-3 (^{3}He) gas is a new magnetic resonance (MR) contrast agent that is being used to study lung functionality. To evaluate the total lung ventilation from the hyperpolarized ^{3}He MR images, it is necessary to segment the lung cavities. This is difficult to accomplish using only the hyperpolarized ^{3}He MR images, so traditional proton (^{1}H) MR images are frequently obtained concurrent with the hyperpolarized ^{3}He MR examination. Segmentation of the lung cavities from traditional proton (^{1}H) MRI is a necessary first step in the analysis of hyperpolarized ^{3}He MR images. In this paper, we develop an active contour model that provides a smooth boundary and accurately captures the high curvature features of the lung cavities from the ^{1}H MR images. This segmentation method is the first parametric active contour model that facilitates straightforward merging of multiple contours. The proposed method of merging computes an external force field that is based on the solution of partial differential equations with boundary condition defined by the initial positions of the evolving contours. A theoretical connection with fluid flow in porous media and the proposed force field is established. Then by using the properties of fluid flow we prove that the proposed method indeed achieves merging and the contours stop at the object boundary as well. Experimental results involving merging in synthetic images are provided. The segmentation technique has been employed in lung ^{1}H MR imaging for segmenting the total lung air space. This technology plays a key role in computing the functional air space from MR images that use hyperpolarized ^{3}He gas as a contrast agent.**

***Index Terms*—Active contour, hyperpolarized gas MRI, image segmentation, merging.**

I. Introduction

A. Medical Imaging Background

TRADITIONAL ^{1}H magnetic resonance imaging (MRI) of the lung is difficult, because the lung consists largely of air, which has a low proton density. A low proton density gives rise to a weak MR signal, but this limitation can be overcome with the use of a new class of contrast agent—hyperpolarized gas. When hyperpolarized helium-3 (H^3He) gas is inhaled, the airspaces fill with the gas, and the gas produces a strong MR signal, allowing a direct assessment of lung ventilation. Using (H^3He), high signal-to-noise ratio images of lung ventilation have been obtained [1]–[8]. Areas of the lung that do not ventilate are deficient in ^{3}He gas and do not produce a MR signal. This lack of ventilation may be caused by airway closure as occurs in asthma or due to tissue destruction as occurs in emphysema. The unventilated areas are, therefore, seen as "defects" or dark areas on the images. Preliminary studies have shown that H^3He lung MRI demonstrates ventilation defects in multiple lung diseases including asthma [1], chronic obstructive pulmonary disease (COPD) [2]–[4] cystic fibrosis [5], [6], smoking related lung disease [2], [4], and bronchiolitis obliterans [7] (Fig. 1).

Other imaging modalities for the lung include computed tomography (CT) and radionuclide ventilation scanning. CT provides information about lung structure but abnormalities of lung ventilation can only be inferred indirectly from changes in structure. Traditional radionuclide ventilation scanning depicts lung ventilation but at lower temporal and spatial resolution than H^3He MRI. H^3He MRI is a promising new technology for functional lung imaging. An open problem for groups working in this field is the quantitative analysis of H^3He MR studies. Currently, a radiologist estimates the percent of the total lung volume that is not ventilated by visually inspecting the images. This method is time consuming and is likely neither precise nor reliable. MRI with H^3He gas as a contrast agent is being used by medical researchers attempting to quantify lung functionality and the effect of pulmonary drugs. Thus, there exists a need for an automated H^3He MRI image analysis method that will be rapid and accurate.

We are developing a system for computing total lung volume and the volume of nonventilated lung from ^{3}He MR studies. From a medical perspective, this effort is the first attempt to quantify ventilation from the H^3He MRI data. Quantification of the H^3He MRI results will be invaluable in analyzing the H^3He scans and correlating the H^3He data with clinical measures of disease. In subjects with severe obstructive lung disease, it is impossible to determine the contour of lung cavity from the H^3He images because large portions of the lung are not ventilated and, therefore, have the same signal as the background on H^3He MRI (Fig. 2). Fig. 2(a) shows a coronal slice of a ^{1}H MR scan of the lung, which provides excellent anatomic detail but no functional information. Fig. 2(b) shows the corresponding H^3He slice, which depicts the regions of the lung that are ventilated (functioning) but no anatomic detail in the nonventilated regions of the lung. Thus, the total lung volume must

Manuscript received June 26, 2002; revised August 22, 2002. The Associate Editor responsible for coordinating the review of this paper and recommending its publication was J. Duncan. *Asterisk indicates corresponding author.*

N. Ray is with the Department of Electrical and Computer Engineering, University of Virginia, Charlottesville, VA 22904 USA.

*S. T. Acton is with the Department of Electrical and Computer Engineering, 351 McCormick Road, University of Virginia, Charlottesville, VA 22904 USA (e-mail: acton@virginia.edu).

T. Altes, E. E. de Lange and J. R. Brookeman are with the Department of Radiology, University of Virginia, Charlottesville, VA 22908 USA.

Digital Object Identifier 10.1109/TMI.2002.808354

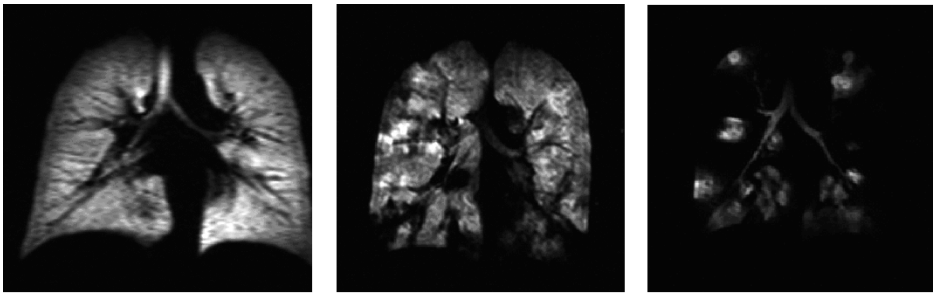

(a) (b) (c)

Fig. 1. Coronal H^3He MR images in three subjects demonstrate homogeneous ventilation in the (a) normal subject and many ventilation defects in the (b) subjects with asthma and (c) Cystic fibrosis. Signal is obtained from the tracheobronchial tree and air spaces of the lung. No signal is obtained from the chest wall or mediastinal structures.

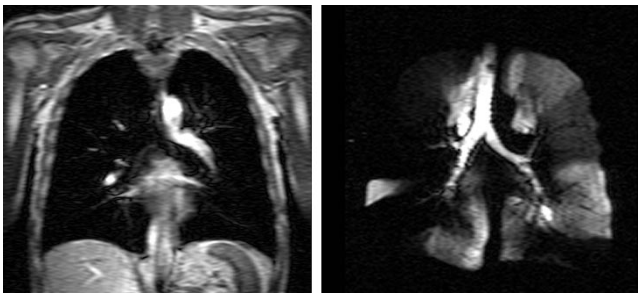

(a) (b)

Fig. 2. (a) ^1H MR image. (b) Corresponding H^3He MR image.

be obtained from the ^1H MRI study, and the volume of ventilated lung must be obtained from the H^3He MRI study. So, to quantify the functional lung air space, we quantitatively compare the lung volume extracted from the proton imagery with the ventilated lung volume extracted from the helium images.

A critical sub-problem in the quantitative analysis of lung functionality, which is the focus of this paper, is the automated segmentation of the ^1H MR images. If the total lung air space is significantly miscalculated, the analysis of the H^3He MR images is rendered useless. The desired result from the ^1H MR segmentation is two smooth contours capturing the boundaries of the two lungs in each slice. At the same time, specific high curvature features, such as the costophrenic angle, must be captured in the segmentation of the ^1H MR images for an accurate calculation of the total lung air space. Active contours, or *snakes* [9], provide an effective vehicle of automated ^1H MR segmentation for the lungs, as the method can always give closed contour as opposed to some adaptive edge detection technique requiring edge linking as postprocessing, e.g., Canny edges [10], moreover desired smoothness of the contour can be obtained by controlling the rigidity of the snake. In this paper, we focus on designing a snake evolution technique for automated ^1H MR segmentation that is robust to contour initialization and allows independent evolution of multiple snakes within a homogeneous region without any requirement for merging them. Note that we are not implementing a multiple-snake procedure that allows splitting of the individual snake.

B. Image Segmentation Background

Parametric curve evolution technique has gained much importance among the image processing and computer vision community after the introduction of active contour or snakes. Numerous applications of snakes include edge detection [9], shape modeling [11], [12], segmentation [13], [14], and motion tracking [13], [15], to mention only a few. In parallel efforts, different gradient-based active contour models and the underlying force fields driving the active contour have been proposed. Examples include balloon and pressure force model [16], distance transform force model [17] and recently gradient vector flow (GVF) model [18], [19]. GVF model outperforms the other gradient-based models in many situations. GVF is capable of attracting the snake from a relatively long distance toward the object edge, i.e., it has a broad capture range; it can also drag the contour inside a long thin cavity [18], [19]. The success of these models mostly depends on the initial contour locations with respect to the object to be segmented. Although the capture range of GVF is very high, even with very a straightforward initial curve, GVF snake fails to recover the object edge. For example, to capture the boundary of a circular object the initial snake must include the center of the circular object [20]. To alleviate the drawback of sensitivity to initial contour placement, in this paper, we propose to modify GVF through adding suitable boundary conditions (BCs) to the partial differential equation (PDE) governing GVF using the initial contour location and the *a priori* knowledge about the object position. We have shown that this modification of GVF helps in alleviating the contour initialization problem in important application specific contexts, e.g., in tracking fast rolling leukocytes from intravital video microscopic images [21], [22] and in finding the lung contours from ^1H MR imagery [20]. As an additional contribution we show here with the help of the porous medium fluid flow analogy that if multiple initial snakes are placed inside a homogeneous region (as in the lung cavity), automatic implicit merging of parametric contours takes place with the proposed modified GVF.

This paper elaborates the lung segmentation application with the use of the proposed modified GVF. Lung cavities have typical intricacies in terms of the high-curvature costophrenic angles and protruding airways, as well as the weak edges appearing mostly at the junction of the left and the right lung cavities. Thus, in certain portions of the lungs the active contour should be capable of recovering the high curvature edges, and in the other portions it should regularize to smooth contour. In a user interactive environment, a snake can be initialized close to the lung outline and the contour can be assigned

different regularization parameters in different segments of the lungs. But the requirement of a high degree of automation for the drug validation study precludes such time-consuming user interactions. Multiple snakes could provide a remedy to this problem when different values of rigidity parameters on different snakes are assigned in an automated way at the beginning of the evolution, from the *a priori* knowledge of the position of the snakes relative to the lung cavities. The snakes evolve all independently of each other without any explicit effort for merging. At the end of the evolution we take the union of all the regions covered by the snakes to obtain the segmented lung cavity.

We point out that the existing successful methods for splitting or merging of parametric active contours [23]–[26] use a combination of the following tasks—combination of: 1) detections of the conditions of merging or splitting; 2) determination of portions of the contour that must be merged; 3) some explicit computations for merging and splitting; and 4) subsequent re-parameterization of the contours. For example, in [23] a triangular decomposition of the rectangular image grid has been performed. With every iteration, the intersections of the contours with the triangular grids are computed that is followed by a decision rule for connecting the intersections among themselves for merging/splitting. In [25], the self-intersections are detected based on the distance between the vertices of the evolving deformable surfaces. [26] also depends on detection of merging/splitting and subsequently applying topological operators to perform actual topological changes. On the contrary, although we are evolving multiple contours inside a homogeneous region, there is no need to explicitly apply any one of the above techniques to achieve merging. In fact, the cost of merging in our proposed method is identical to the computational cost of a nonmerging scenario. The proposed method can be summarized in the following four steps.

1) Initial snakes are placed automatically within the lung cavities that are to be segmented. Coarse scale image registration can be employed to ensure that initial snakes are placed within the lung cavity.
2) The external force field for evolving the snakes is computed by solving PDEs with Dirichlet BC [27] based on the initial snakes.
3) All snakes are evolved independently of each other (preferably in parallel) with the external force developed in 2).
4) At the end of active contour evolution, the desired segmentation is obtained as the union of the regions covered by all the snakes.

We also like to point out that the proposed modified GVF flow can even be applied to evolve geometric contours within the level set paradigm [28]. Then, changes in topology can be accommodated automatically. However we prefer to use parametric active contours as to demonstrate that their merging within a homogeneous regions is taken care of implicitly and automatically here. Synthetic experiments are provided to demonstrate the merging capability and to show the insensitivity of our method to initial snake position. The proposed technique has been successfully applied to ^{1}H MR images to compute the total lung air space. These results in turn are used to compute the functional lung air space from the hyperpolarized helium MRI, which can be utilized in studies monitoring the efficacy of pulmonary drugs, for example.

Organization of this paper is as follows: Section II gives the necessary background about snakes or active contours. In Section III-A, we discuss the proposed segmentation method. In Section III-B, we establish the connection with a fluid flow. Section IV-A provides synthetic experiments that demonstrate parametric snake merging, while Section IV-B details the aspect of snake initialization and compares the proposed method with existing snake evolution forces. Section IV-C demonstrates application of the proposed technique to MRI segmentation and is followed by conclusions in Section V.

II. Parametric Active Contours

An active contour or a snake can be an open or a closed elastic curve defined on the image domain. A snake moves on the domain according to the influence of internal forces as well as by the external forces computed from the image data. The internal forces typically include the resistance to bending and stretching of the snake. The external forces are often so defined that the snake conforms to object edges, such as the lung boundary. A parametric active contour or snake is a curve $\mathbf{C}(s) = (p(s), q(s))$ defined via the parameter $s \in [0, 1]$. The point $\mathbf{C}(s)$ is sometimes referred to as a *snaxel*. The snake is evolved (moved) in such a way that minimizes an energy functional [9], [18], [19]

$$E_s = \int_0^1 \left(\frac{1}{2} \left\{ \alpha |\mathbf{C}'(s)|^2 + \beta |\mathbf{C}''(s)|^2 \right\} + E_{\text{ext}}[\mathbf{C}(s)] \right) ds \tag{1}$$

where internal energy is represented by the first term in the integral and the external energy is given by E_{ext}. The nonnegative constants α and β are the rigidity parameters expressing the resistance to stretching and to bending of the active contour, respectively. $\mathbf{C}'$ and $\mathbf{C}''$ represent the first and the second derivative of the snake with respect to the parameter s. The external energy term E_{ext} is usually defined as $-|\nabla G_\sigma(x, y) * I(x, y)|$, where $I(x, y)$ is the image intensity at (x, y), $G_\sigma(x, y)$ is the two-dimensional (2-D) Gaussian kernel with σ as standard deviation [18]. The energy functional (1) can be minimized by employing the principles of variational calculus to obtain the following Euler equations [9]

$$\alpha \mathbf{C}''(s) - \beta \mathbf{C}''(s) - \nabla E_{\text{ext}}(\mathbf{C}(s)) = 0 \tag{2}$$

where $\mathbf{C}''$ and $\mathbf{C}''''$ are the second and fourth derivatives of the curve with respect to the parameter s. Equation (2) may be looked upon as force-balance equations where the external force $-\nabla E_{\text{ext}}(\mathbf{C}(s))$ is balanced against the internal force $\alpha \mathbf{C}''(s) - \beta \mathbf{C}''(s)$ [18]. By solving (2), one computes the desired snake that minimizes the energy functional (1). In order to solve (2), the snake is treated as a function of time t, as well as of the parameter s, i.e., $C(s, t)$. Then the partial derivative of $\mathbf{C}$ with respect to time t is computed using

$$\mathbf{C}_t(s, t) = \alpha \mathbf{C}''(s, t) - \beta \mathbf{C}''''(s, t) + \mathbf{v}(\mathbf{C}(s, t)) \tag{3}$$

where the external force is denoted by $\mathbf{v}$. The desired solution of (3) is a stationary state solution that is obtained when the term

$\mathbf{C}_t(s,t)$ vanishes. In general, (3) is solved in steepest descent manner. Thus, the process starts with an initial guess (i.e., an initial contour) and evolves toward the final solution, driven by both external and internal forces.

The success of the snake segmentation technique depends on the design of the external force $\mathbf{v}$ by which the snake is guided. The gradient magnitude of image gradient as an external force is already defined. A serious limitation of using gradient magnitude alone is that the energy-minimizing snake will miss the object edge unless it is initialized very close to the object edge. To solve this problem, a pressure force model can be used to expand the snake as though it were a balloon [16]. This inflating force is balanced by the image gradient force, and, when the snake position coincides with an object boundary, the snake movement may be halted. One drawback of the pressure force model is that it may become strong enough to ignore the image gradient force in weak object edges [18].

Another force model is the *distance potential force* proposed by Cohen and Cohen [17]. In this case, the value of the distance map is computed as the distance between the pixel and the closest boundary point. Though it improves upon the previous two force models, the distance potential force lacks the capability of guiding the snake into long object cavities [18] such as the lung costophrenic angle. Xu and Prince have developed the GVF and generalized GVF (GGVF) to overcome the above-mentioned difficulties [18], [19]. These forces are obtained as a solution of two decoupled PDEs. Our proposed method relies on these GGVF PDEs along with a Dirichlet BC based on initial snake positions for the purpose of designing the snake force. This proposed external force has the capability to merge snakes within a homogeneous image region such as the lung cavity.

III. Merging Active Contours

A. Partial Differential Equations Used for Active Contour Evolution

To effectively capture the high curvature regions of the lung and to preserve the smoothness of the boundary, we propose the use of multiple parametric snakes that have the ability to merge. We design the external guiding force for the snake in such a way that two nonintersecting as well as growing active contours never cross each other and never leave any space between contours unless an object exists in between. Additionally we require that the growing snakes stop at the object boundary. In this regard, we propose a force field that is computed on the image domain by solving GGVF PDEs with the BCs based on the initial snakes. To illustrate the proposed external snake-driving force let us first consider the GGVF PDEs [19]

$$\mathbf{v}_t = g(|\nabla f|)\nabla^2\mathbf{v} - h(|\nabla f|)(\mathbf{v} - \nabla f) \tag{4}$$

where ∇^2 is the Laplacian operator. The functions g and h are defined as

$$g(|\nabla f|) = e^{-(|\nabla f|/K)}, \quad h(|\nabla f|) = 1 - g(|\nabla f|) \tag{5}$$

where K is a user defined parameter controlling the degree of smoothness of the snake external force field, and $f(x,y)$ is defined as the "edge map" and is equal to $|\nabla G_\sigma(x,y) * I(x,y)|$ [18]. Now, let us assume that within a homogeneous region of the image we have placed n initial snakes, and we evolve the snake positions according to (3). Let us further assume that these initial contours represent n nonconnected closed regions D having boundary ∂D. We add the following BC of the Dirichlet type on the PDEs (4):

$$\begin{aligned} \mathbf{v}(x,y) &= \mathbf{0} \text{ for } (x,y) \in D, \\ \mathbf{v}(x,y) &= \mathbf{n}(x,y), \text{ for } (x,y) \in \partial D \end{aligned} \tag{6}$$

where $\mathbf{n}(x,y)$ is the unit outward normal at (x,y) on the image domain boundary ∂D.

In essence, we treat the initial snakes as sources emitting unit normal vectors on the image domain. Solving the PDE (4) along with BC (6) results in the required guiding force for the snakes with merging capability. Thus, we diffuse the gradients of the edge map and the outward normal vectors defined on the initial snakes. It can be shown that this system of PDEs with the given BC has a unique nontrivial solution [27]. This system can also be easily discretized with finite difference scheme [19], [27]. Owing to the competitive nature of the diffusion process, the field $\mathbf{v}$ is constructed in such a way that between two or more growing snakes there is a separating streamline. So, the evolving snakes moving under the influence of $\mathbf{v}$ never cross each other. Instead, the snake stops at the interface with a competing snake, giving the desired effect—the merging of parametric snakes. The Section III-B details this approach. In Section III-B, we also establish a connection to fluid flow in a porous medium with the proposed flow.

B. Analysis of Active Contour Merging

In this section, we first analyze the proposed guiding force vector field from the angle of fluid dynamics and with the help of some elementary properties of fluid flow we show that merging of active contours is indeed achievable. To do so, we first note that the PDE in (4) that generates the force vector field $\mathbf{v}(x,y) = (u(x,y), v(x,y))$, can be rewritten in the following way:

$$\begin{aligned} u_t &= g(|\nabla f|)\nabla^2 u - h(|\nabla f|)(u - f_x) \\ v_t &= g(|\nabla f|)\nabla^2 v - h(|\nabla f|)(v - f_y) \end{aligned} \tag{7}$$

where (u,v) is the 2-D flow and (f_x, f_y) is the gradient of f, i.e., ∇f. Though Xu and Prince have considered the process in (7) as generalized diffusion equations [18], [19], we will see in a moment that the equations are the Navier–Stokes equations for a viscous incompressible fluid. Later on, this equivalence will help us prove that merging is achieved. The Navier–Stokes equations in such a case can be written as [29]

$$\begin{aligned} u_t + \left(u\frac{\partial u}{\partial x} + u\frac{\partial u}{\partial y}\right) &= \frac{\eta}{\rho}\nabla^2 u - \frac{1}{\rho}\frac{\partial p}{\partial x} \\ v_t + \left(u\frac{\partial v}{\partial x} + v\frac{\partial v}{\partial y}\right) &= \frac{\eta}{\rho}\nabla^2 v - \frac{1}{\rho}\frac{\partial p}{\partial y} \end{aligned} \tag{8}$$

where as usual (u,v) is the flow velocity, p is the fluid pressure, η is the Newtonian viscosity coefficient and ρ is the fluid density. In general, for low Reynolds numbers the nonlinear terms in

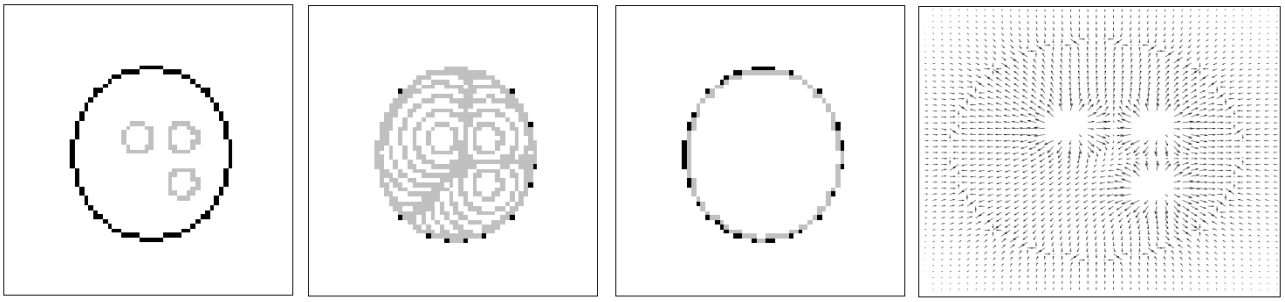

(a) (b) (c) (d)

Fig. 3. (a) Circle image with three initial snakes inside the circle. (b) Evolution of the snakes under the proposed guiding force. (c) Elimination of common boundaries leads to the proper delineation of the circle. (d) Proposed snake-guiding force field on the circle image with three initial snakes.

the parenthesis of the left hand side of (8) can be neglected [29]. Then the Navier–Stokes equations take the following form:

$$u_t = \frac{\eta}{\rho}\nabla^2 u - \frac{1}{\rho}\frac{\partial p}{\partial x}$$
$$v_t = \frac{\eta}{\rho}\nabla^2 v - \frac{1}{\rho}\frac{\partial p}{\partial y}. \tag{9}$$

We now see that (7) and (9) have the same form, provided in (9) we let $\partial p/\partial x = u - f_x$ and $\partial p/\partial y = v - f_y$. This closely resembles flow of fluid through a porous medium where the flow velocity is proportional to the pressure gradient [30]. The term $(\partial p/\partial x, \partial p/\partial y)$ can be thought of as the shearing force acting on unit volume of the fluid. Now the intuition behind considering GGVF as a flow becomes quite clear. If we place some marker particles in the fluid flow, we can follow them to see where they remain at rest. If a particle is under the influence of two opposing flows of equal strengths, it remains at rest. These regions are called local "sinks." The object edges are the locations where two opposing flow velocities nullify each other. So naturally, the marker particles cling to the object edge.

The snake exactly serves the purpose of detecting boundaries such as with lung segmentation from ^{1}H MRI. We can think of the snake as a chain of marker particles immersed in the fluid. Snake evolution merely simulates the motion of the marker particles. There are at least two advantages of evolving snake as compared with evolving isolated particles. If the flow lines are followed by some marker particles, then two closely placed particles eventually either separate or join. A snake/active contour does not encounter this dilemma as it retains connectivity as two neighboring snaxels separate. Also, an active contour model allows deletion of closely spaced snaxels. The snake itself has some rigidity—resistance to bending and stretching, i.e., some internal elastic properties. The internal properties allow a regularized segmentation with smooth boundaries, as will be demonstrated on the MR imagery.

Let us first illustrate how merging occurs with the help an example. Fig. 3(a) contains a circle (black) and three initial snakes (gray) placed inside the circle. Fig. 3(b) shows that at the end of the evolution we are left with three regions due to the three snakes. Fig. 3(c) depicts the boundary of the merged snakes, i.e., after taking union of the three regions contributed by the snakes. Fig. 3(d) illustrates the force field that is obtained by solving (4) along with the imposed BC (6). In Fig. 3(d), the three circular gaps correspond to the three initial snakes of Fig. 3(a). We observe that streamlines are generated at these inside hole-boundaries and they end up in the outer circle in the Fig. 3(d) that corresponds to the circle of the image in Fig. 3(a). So the initial contours act as sources and the outside boundary acts as a sink as in a 2-D fluid flow field. In Fig. 3(d), we also observe the presence of *stagnation* points. These points are located in between sources where flow velocity is zero. We see that some of the streamlines generated from sources end up in stagnation points and more interestingly some streamlines are generated from the stagnation points and end up in sink, i.e., the object boundary. Streamlines of latter type are called *separation* streamlines.

To explain the basis behind the merging process we use the following properties from elementary fluid mechanics (e.g., see [31]).

- **Property 1:** In a laminar type fluid flow (flow at low Reynolds number), fluid particles follow certain paths in the flow. Such paths are called streamlines. *Any two streamlines in a laminar type fluid flow never cross each other*.
- **Property 2:** Sources and sinks in a flow field are flow discontinuities where streamlines generate and end, respectively.
- **Property 3:** *Between two sources there will be stagnation point(s), where the flow velocity is zero*. Streamlines generated from stagnation points are called separating streamlines. So, between two sources there will always be separating streamlines.

Before we give the proof of merging, let us define an object boundary as an extended local sink in the flow field where the streamlines terminate. This definition is on par with the equivalence of the fluid flow and the proposed force field. Now, we prove the following proposition, which plays a key role in the proof of merging.

Proposition 1: If a number of sources, C_1, C_2, C_3, ..., are placed inside an extended local sink, S, in a 2-D laminar type fluid flow field, then each source C_i will define a 2-D region R_i in such a way that: 1) C_i is totally inside R_i; 2) given a point (x, y) in R_i but not inside C_i, there will be a unique streamline passing through (x, y) generated from C_i; 3) if $i \neq j$ then $R_i \cap R_j = \emptyset$; 4) for two *side by side* sources C_i and C_j in a homogeneous region, the regions R_i and R_j will become arbitrarily close to each other. Two snakes are said to be "side by

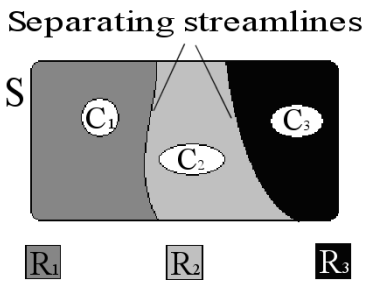

Fig. 4. Sources, sink, initial snakes, regions, and separating streamlines.

side" if a straight path exists connecting the two contours that is uninterrupted by another snake. Note that the interior of a homogeneous region does not contain sinks.

Proof: For the shake of explanation, Fig. 4 illustrates the initial snakes or the sources (C_is), the object or the sink (S). Let (x, y) be a point that is completely inside S but outside all the initial snakes, i.e., C_is. Then by the continuity of the fluid flow [29] there must exist a streamline that passes through this point (x, y). If the point (x, y) is not on the separating streamline then **Property 2** asserts that the streamline through (x, y) must have been generated from a source C_i. So we define the region corresponding to C_i as R_i in the following way: R_i is the 2-D region where all the streamlines generated from C_i will pass through. This construction of the region R_i proves 1) and 2) of **Proposition 1.** Fig. 4 shows such regions R_is.

We prove 3) by contradiction, let a point $(p, q) \in R_i \cap R_j$. Then there exists a streamline generated from the source C_i passing through (p, q) and there is another streamline generated from C_j and passing through (p, q). But this is precluded by **Property 1**. So $R_i \cap R_j = \emptyset$.

To prove 4), let us consider **Property 3** that asserts that there will be a stagnation point between two side by side sources C_i and C_j. From this stagnation point, a separating streamline will be generated and will end up in another stagnation point or the sink. Any streamline generated from C_i or C_j cannot cross this separating streamline, but will only be arbitrarily close to the separating streamline by virtue of the fluid continuity property. So the separating streamline acts as a common boundary for the two regions R_i and R_j. Since a streamline is actually arbitrarily thin, the two regions R_i and R_j are arbitrarily close to each other. Q.E.D.

Thus, **Proposition 1** finally validates our claim that by the proposed method of snake evolution, two side-by-side placed snakes never cross each other, but comes arbitrarily close to each other in other words they touch each other. This also proves that we can let the all the snakes evolve and then finally take the union of the regions covered by them to get the desired segmentation.

IV. Results

A. Synthetic Experiments of Contour Merging

The purpose of this section is to show experimentally that the proposed method does not depend on the number, the shape, the size and the position of the initial snakes. Fig. 5(a) shows 25 initial circular snakes inside a circle image. All of the circular snakes have randomly selected radii within the range of 2–8 pixels and are also placed randomly (uniformly distributed) inside the circle. The only constraint is that no two initial snakes overlap. The final evolution has led to the configuration shown in Fig. 5(b). Taking the union of 25 regions of Fig. 5(b), contributed by 25 snakes we obtain the result shown in Fig. 5(c), where the circle boundary has been correctly captured after merging. In Fig. 5(d), the same circle image is initialized with 50 snakes with random radii and positions. Fig. 5(e) shows the final stage after evolution. Fig. 5(f) illustrates the capturing of the circle after collecting the tiny regions of Fig. 5(e). In both cases, merging has produced correct segmentation.

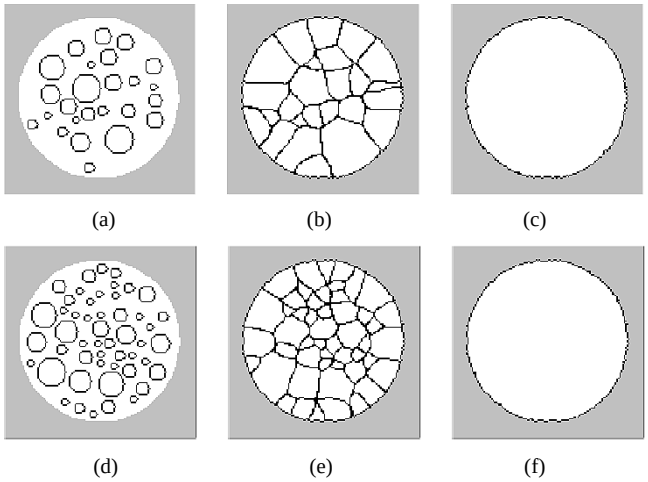

Fig. 5. (a) Twenty-five initial snakes in the circle image. (b) Evolution of 25 snakes inside the circle. (c) Taking the set union of regions in (b) leads to capturing the outer circle. (d) Fifty initial snakes in the circle image. (e) Evolution of 50 snakes inside the circle. (f) Union of regions in (e) leads to capturing the circle.

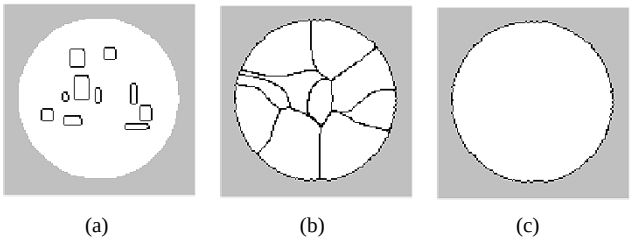

Fig. 6. (a) Ten rectangular initial snakes in the circle image. (b) Configuration after evolution of rectangular shaped initial snakes. (c) Final segmentation after taking union of ten regions of (b).

In the next experiment, we show the same circular shape can be captured if one starts with rectangular type initial shapes. Fig. 6(a) shows ten rectangular shaped initial snakes having dimensions chosen randomly with uniform distribution between 2 and 12 units. Their positions are also chosen randomly as before. Fig. 6(b) illustrates the final state after evolution of these initial rectangular snakes. Fig. 6(c) shows that taking union of the regions of Fig. 6(b) has correctly led to the circular shape of the object. The synthetic experiments do not validate the active contour method for MRI lung cavity segmentation, but the experiments do support the claim that the method is insensitive to initial contour conditions within ideal homogeneous regions.

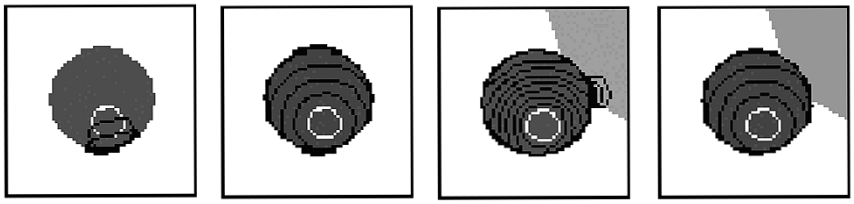

(a) (b) (c) (d)

Fig. 7. (a) Initial snake (white contour) and evolution by GVF (black contours). (b) Initial snake (white contour) and proposed snake evolution (black contours). (c) Initial snake (white contour) and snake evolution by pressure force (black contours). (d) Initial snake (white contour) and proposed snake evolution (black contours).

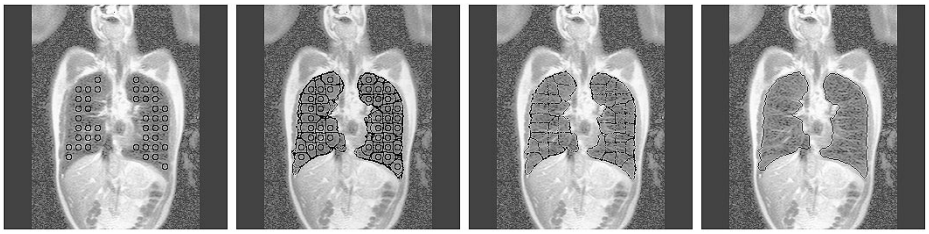

(a) (b) (c) (d)

Fig. 8. (a) Initial snakes inside a 2-D slice. (b) Evolution of the snakes. (c) Final configuration of the snakes. (d) Segmentation taking union of the regions bounded by the snakes in (c).

B. Comparison With the Other Methods

The comparison given in this section shows the difference of our approach with the GGVF approach of Xu and Prince [19] and with the pressure force approach [16]. Adding the BC to the GGVF PDEs allows the proposed method superior performance with respect to the initial snake placement. Fig. 7(a) shows a circle image with one initial snake (white contour), which does not include the center of the circular object. Fig. 7(a) also shows the GGVF snake evolution, where we notice that the snake has collapsed to one side of the object boundary. The reason behind the failure of the existing GGVF method is clear. Since GGVF defines a medial axis of an object [32], the initial snake must include the medial axis in order to capture the desired object. As the medial axis in this case is the center of the circle, the GGVF snake fails to capture the circular object. There is no such concern with respect to the initial snake placement in the proposed snake evolution technique. Fig. 7(b) shows that with the same initial position (white contour) the snake with the proposed technique correctly recovers the circle object. The only constraint in case of the proposed technique is that the object should include the initial snake(s), but the snakes themselves do not need to include the medial axis. This relaxed constraint is more suitable for a number of applications, including the lung segmentation discussed in Section IV-C.

Fig. 7(c) and (d) compare the proposed method with the pressure/balloon force. We observe that the pressure snake leaks through the low contrast edges, whereas the proposed snake method survives both the weak and the strong edges.

C. Determination of Lung Ventilation by Merging Snakes

The analysis of lung ventilation by way of hyperpolarized gas MRI is emerging as a useful clinical tool [8]. Quantification of lung functionality through the use of the MRI techniques can be used to measure the usefulness of respiratory-related drugs [8]. From the proton images (^{1}H MRI), the radiologists segment the total lung cavity. Then, they use the Helium images (MR imagery where ^{3}He is inhaled) to compute the ventilated portions of the lungs. In Fig. 2(a), one 2-D slice of the proton imagery is provided and in Fig. 2(b) the corresponding ^{3}He slice is shown. The ratio of volume computed from the helium imagery (yielding functional volume) and the cavity volume computed from the proton imagery can be used to calculate percent ventilation, which in turn can be used to measure lung disease severity. For the purpose of pulmonary drug validation, hundreds of MRI slices needs segmentation, when done by the radiologists it typically takes a couple of days. So there is crucial requirement of automating the system.

We have applied the proposed merging method to capture total lung cavity space in proton MRI slices. Capturing lung cavities in each of the slices is necessary to obtain the total lung cavity volume. For the proposed method, the initialization of snakes is advantageous over the same in GGVF, because the proposed method alleviates the need to include the medial axis of the lung cavity, a requirement that would be difficult to automate for each MRI slice. We first obtain a crude segmentation through some standard edge detection process, and then place the snakes in such way that they do not hit any extended edge (which possibly belong to the lung boundaries). For the MRI slices, we roughly know the positions of the lungs. We effectively use this prior knowledge in placing the initial snakes as well. In other words, in placing the initial snakes one only has to ensure that they are not outside the lung cavities, no matter if they include the medial axes or not. Fig. 8(a) shows the initial tiny snakes placed inside the lung cavities. Fig. 8(b) shows the evolution of the snakes. Fig. 8(c) shows the final configuration of the snakes after evolution has stopped. Fig. 8(d) shows the final segmentation result after taking the union of the regions bounded by all the snakes in Fig. 8(c). In Fig. 9(a)–(n), we show

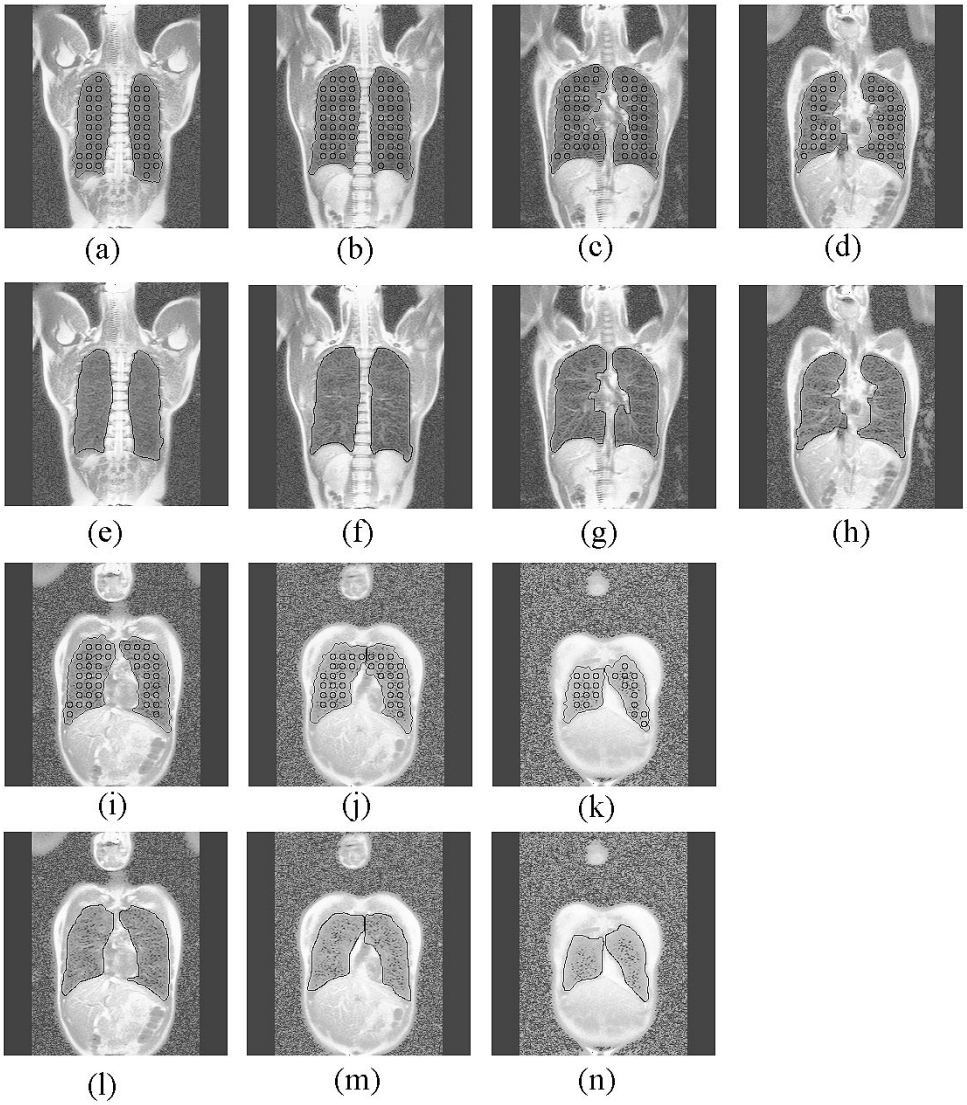

Fig. 9. (a)-(d) and (i)-(k) Initial snakes (small black circles) and final segmentation. (e)-(h) and (l)-(n) Corresponding ground truth contours.

every alternate slice of a test MR data sequence with segmentation contours found by the proposed algorithm and radiologists.

Multiple snakes aid the evolution process in a number of ways. Being able to evolve completely independent of each other, multiple snakes are able to evolve in parallel on a multiprocessor machine, saving evolution time when compared with the single snake approach. Besides that we may effectively exploit the independent nature of the snakes by assigning different values to the rigidity parameters in them. As for example, to capture the costophrenic angles the lower most snakes are assigned relaxed rigidity parameters than the upper snakes [see Fig. 8(d) for example]. This is particularly advantageous in an automated environment like the application at hand. This eliminates any user interaction to assign different values of the rigidity parameters to different contour segments of a single parametric snake to achieve the same task. Another advantage of multiple snake evolution is as follows. Sometimes a single snake cannot capture the whole object as the region may lack sufficient homogeneity, in these cases multiple snakes come to rescue. Fig. 10 illustrates this point. Here the same proton MRI slice is initialized with a single snake. The same parameters as used in multiple snake case are used for setting up the GGVF flow with proposed BCs and the same set of snake parameters are used for the snake evolution. The snake is not able to capture the entire lung (see Fig. 10).

Fig. 10. An example in which single snake evolution fails to capture the lung cavities.

To emphasize the effectiveness of the proposed technique with respect to the segmentation of lung cavities, we have utilized Pratt's figure of merit (FOM) [33]. The FOM is a dimensionless number between zero and one. A maximum attainable

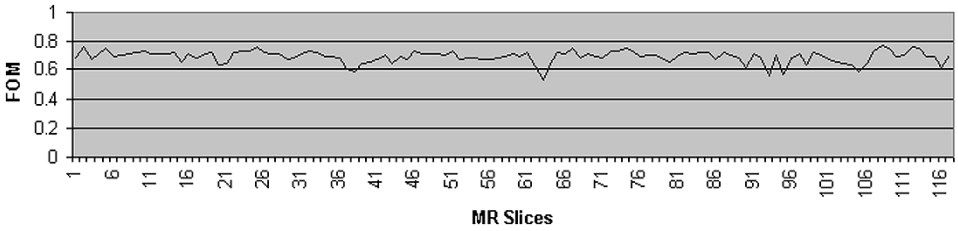

Fig. 11. Pratt's FOM for lung segmentation of the 2-D MR slices.

Fig. 12. Percentage error of segmentation.

TABLE I
PRATT FOM FOR THE PROPOSED METHOD

MRI Data sets	FOM with the Proposed method
1	0.7085
2	0.7059
3	0.7120
4	0.6502
5	0.6983
6	0.6665
7	0.7156
8	0.6860
9	0.6617
10	0.7076

TABLE II
PERCENTAGE ERROR IN LUNG TOTAL SPACE SEGMENTATION

MRI data sets	Percentage error in segmentation
1	6.14
2	5.94
3	5.32
4	9.01
5	6.35
6	5.13
7	4.46
8	6.00
9	7.95
10	4.05

FOM will be one for an ideal segmentation. The FOM quantifies the comparison between ideal edges and detected edges of an image. This basically gives us an idea about the quality of edges detected on an image in terms of their localization as well as absence of extra edges. As the FOM requires knowledge of ideal edges as ground truth, we have used manual segmentation data provided by radiologists. Now the FOM of the proposed segmentation is computed based on this ground truth set. We have carried out automated segmentation on ten MRI data sets. Fig. 11 shows the FOMs obtained on all the MRI slices over the ten data sets. Table I summarizes the result by showing the mean FOMs obtained on each MRI data set.

Percentage error has also been computed as another performance measure defined as

$$\text{Error}_{\text{seg}} = \frac{\sum_{i,j} |I(i,j) - I_g(i,j)|}{\sum_{i,j} I_g(i,j)} x100\%$$

where the segmented image $I(i,j)$ and ground truth image $I_g(i,j)$ are both binary images having value one inside lung and zero outside. Fig. 12 shows the percentage errors on all the slices over the ten MRI data sets. Table II summarizes the segmentation performance by showing the mean percentage errors for the ten data sets.

After computing the lung cavity space from the proton imagery with the proposed active contour method, we compute the functional lung air space from the ^{3}He imagery. We take the final evolved snake contours from proton image slice and register them to the corresponding helium image slice. We then classify the zone of the helium image slice that is within the computed contour into three classes (as directed by the UVa radiologists for these images) by fuzzy c-means classification [34]. The classification is unsupervised and is performed on the original unprocessed data. An example classification is shown in Fig. 13(a). The two classes with higher associated mean intensity values (normally ventilated and hypoventilated regions) are combined to form the lung air space as shown in Fig. 13(b). Now the functional lung air space ratio is calculated as the ratio of lung air space to total lung space. Fig. 13(c) shows functional lung air space obtained on a posttreatment image slice. Fig. 13(a)–(c) also shows the overlaid snake contours from the proposed evolution technique.

As an example of the possible clinical application of such a technique, we have calculated the functional lung air space ratio for each of the slice both in post and pretreatment scenarios for bronchodilation. Toward this end, we have provided results for the entire set of volumetric slices within one study. For each

(a) (b) (c)

Fig. 13. (a) Classification of ^{3}He MRI slice within the total lung space enclosed by contours. (b) Combination two classes to form functional lung air space. This is a pretreatment lung image. (c) Functional lung space for a posttreatment lung MRI ^{3}He slice.

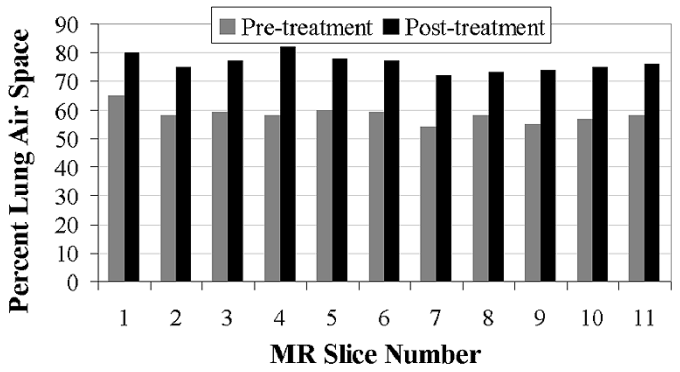

Fig. 14. Functional air space for pretreatment and posttreatment lungs.

of the image pairs (^{1}H MR image and the corresponding ^{3}He MR image), the functional lung air space ratio is calculated. Thus, we can compute the functional lung air space ratio for the entire volumetric MRI set. To compare these functional lung air space ratios in pretreatment and posttreatment scenario, we compute the functional lung air space ratio in both these cases and have plotted the comparative graphs in Fig. 14. The functional lung air space ratio in each of the posttreatment slices is significantly greater than that in the corresponding pretreatment slice. From this graph, the efficacy of the treatment may be observed. The example encourages the possibility of using our technique clinically.

V. Conclusion

From a medical image processing perspective, we have introduced a novel technique for merging parametric active contours within closed homogeneous image region for MRI segmentation. We have further analyzed the proposed technique in the light of fluid dynamics. This theoretical insight has helped us prove that merging of contours is indeed performed by the proposed technique. The fluid flow model also explains why the GGVF external force technique has been quite successful for evolving active contours in complex applications.

Further, we have successfully applied the technique to MRI data for the purpose of lung ventilation analysis. From the clinical perspective, this is a necessary first step in the attempt to quantify the lung functional space through the use of hyperpolarized gas MR imagery. To facilitate the computation of functional air space, the segmentation of ^{1}H MR imagery is required. The active contour method with the merging capability is well matched to the problem of delineating the lung cavities.

Acknowledgment

The authors would like to thank Dr. J. Knight-Scott of the University of Virginia, Department of Biomedical Engineering for advice and direction in processing MR images. N.Ray would like to expresses his deep gratitude to Dr. A. K. Chattopadhyay of the Max-Planck-Institute for the Physics of Complex Systems, Dresden, Germany, for establishing the connection with fluid flow equations.

References

[1] T. A. Altes, P. L. Powers, J. Knight-Scott, G. Rakes, T. A. E. Platts-Mills, E. E. de Lange, B. A. Alford, J. P. Mugler, and J. R. Brookeman, "Hyperpolarized ^{3}He lung ventilation imaging in asthmatics: Preliminary results," JMRI, 2001, to be published.

[2] E. E. de Lange *et al.*, "Lung air spaces: MR imaging evaluation with hyperpolarized ^{3}He gas," *Radiology*, vol. 210, pp. 851–857, 1999.

[3] H. Middleton *et al.*, "MR imaging with hyperpolarized ^{3}He gas," *MRM*, vol. 33, pp. 271–275, 1995.

[4] J. R. MacFall *et al.*, "Human lung airspaces: Potential for MR imaging with hyperpolarized ^{3}He," *Radiology*, vol. 200, pp. 553–558, 1996.

[5] H. U. Kauczor *et al.*, "Normal and abnormal pulmonary ventilation: Visualization at hyperpolarized He-3 MR imaging," *Radiology*, vol. 201, pp. 564–568, 1996.

[6] H. U. Kauczor *et al.*, "Imaging of the lungs using ^{3}He MRI: Preliminary clinical experience in 18 patients with and without lung disease," *JMRI*, vol. 7, pp. 538–543, 1997.

[7] L. F. Donnelly *et al.*, "Cystic fibrosis: Combined hyperpolarized ^{3}He-enhanced and conventional proton MR imaging in the lung-preliminary observations," *Radiology*, vol. 212, pp. 885–889, 1999.

[8] H. Middleton *et al.*, "MR imaging with hyperpolarized He-3 gas," *Magn. Reson. Med.*, vol. 33, pp. 271–275, 1995.

[9] M. Kass, A. Witkin, and D. Terzopolous, "Snakes: Active contour models," *Int. J. Comput. Vis.*, vol. 1, pp. 321–331, 1987.

[10] J. Canny, "A computational approach to edge detection," *IEEE Trans. Pattern Anal. Machine Intell.*, vol. PAMI-8, pp. 679–698, Nov. 1986.

[11] D. Terzopoulos and K. Fleischer, "Deformable models," *Vis. Comput*, vol. 4, pp. 306–331, 1988.

[12] T. McInerney and D. Terzopoulos, "A dynamic finite element surface model for segmentation and tracking in multidimensional medical images with application to cardiac 4D image analysis," *Comput. Med. Image. Graph.*, vol. 19, pp. 69–83, 1995.

[13] F. Leymarie and M. D. Levine, "Tracking deformable objects in the plane using an active contour model," *IEEE Trans. Pattern Anal. Machine Intell.*, vol. 15, pp. 617–634, June 1993.

[14] R. Durikovic, K. Kaneda, and H. Yamashita, "Dynamic contour: A texture approach and contour operations," *Vis. Comput.*, vol. 11, pp. 277–289, 1995.

[15] D. Terzopoulos and R. Szeliski, *Tracking With Kalman Snakes*, A. Blake and A. Yuille, Eds. Cambridge, MA: Active Vision, MIT Press, 1992, pp. 3–20.

[16] L. D. Cohen, "On active contour models and balloons," *CVGIP: Image Understanding*, vol. 53, pp. 211–218, 1991.

[17] L. D. Cohen and I. Cohen, "Finite-element methods for active contour models and balloons for 2-D and 3-D images," *IEEE Trans. Pattern Anal. Machine Intell.*, vol. 15, pp. 1131–1147, Nov. 1993.

[18] C. Xu and J. L. Prince, "Snakes, shapes, and gradient vector flow," *IEEE Trans. Image Processing*, vol. 7, pp. 359–369, 1998.

[19] ——, "Generalized gradient vector flow external forces for active contours," *Signal Process.*, vol. 71, pp. 131–139, 1998.

[20] N. Ray, S. T. Acton, T. Altes, and E. E. de Lange, "MRI ventilation analysis by merging parametric active contours," in *Proc. IEEE ICIP 2001*, pp. 861–864.

[21] N. Ray, S. T. Acton, and K. F. Ley, "Tracking leukocytes *in vivo* with shape and size constrained active contours," *IEEE Trans. Med. Imag. (Special Issue on Image Analysis in Drug Discovery and Clinical Trials)*, vol. 21, pp. 1222–1235, Oct. 2002.

[22] N. Ray and S. T. Acton, "Tracking fast-rolling leukocytes *in vivo* with active contours," in *Proc. IEEE ICIP 2002*, sec. III, pp. 165–168.

[23] T. McInerney and D. Terzopolous, "T-snakes: Topology adaptive snakes," *Med. Image Anal.*, vol. 4, pp. 73–91, 2000.

[24] F. Leitner and P. Cinquin, "Complex topology 3D objects segmentation," in *SPIE Conf. Advances in Intelligent Robotics Systems*, vol. 1609, Boston, MA, Nov. 1991.

[25] J.-O. Lachaud and A. Montanvert, "Deformable meshes with automated topology changes for coarse-to-fine three-dimensional surface extraction," *Med. Image Anal.*, vol. 3, no. 2, pp. 187–207, 1999.
[26] H. Delingette and J. Montagnat, "Topology and Shape Constraints on Parametric Active Contours," INRIA, Paris, France, Tech. Rep.3880, 2000.
[27] C. A. Hall and T. A. Porsching, *Numerical Analysis of Partial Differential Equations*. Englewood Cliffs, NJ: Prentice-Hall, 1990.
[28] J. A. Sethian, *Level Set Methods and Fast Marching Methods*. Cambridge: Cambridge University Press, 1999.
[29] L. D. Landau and E. M. Lifshitz, *Fluid Mechanics*. Elmsford, NY: Pergamon, 1975.
[30] J. Bear, *Dynamics of Fluids in Porous Media*. New York: Dover, 1988.
[31] I. H. Shames, *Mechanics of Fluids*. New York: McGraw-Hill, 1992.
[32] S. Osher, "Level set based algorithms for image restoration, surface interpolation and solving PDE's on general manifolds with applications to image processing and computer graphics," presented at the *34th Asiomar Conf. Signals, Systems, and Computers*, Pacific Grove, CA, Oct. 29–Nov. 1 2000.
[33] W. K. Pratt, *Digital Image Processing*. New York: Wiley, 1991.
[34] J. C. Bezdek, J. Keller, R. Krisnapuram, and N. R. Pal, *Fuzzy Models and Algorithms for Pattern Recognition and Image Processing*. Boston, MA: Kluwer Academic, 1999.